

On the Physical Origins of the Millimeter Fundamental Plane in Active Galactic Nuclei

KRATIKA MAZDE,¹ ANGELO RICARTE,^{2,3} AND GEORGE N. WONG^{4,5}

¹*Institut d’Astrophysique de Paris, CNRS & Sorbonne Université, UMR 7095 98 bis boulevard Arago, 75014, Paris, France*

²*Center for Astrophysics / Harvard & Smithsonian, 60 Garden Street, Cambridge, MA 02138, USA*

³*Black Hole Initiative, Harvard University, 20 Garden Street, Cambridge, MA 02138, USA*

⁴*Princeton Gravity Initiative, Princeton University, Princeton, NJ 08544, USA*

⁵*School of Natural Sciences, Institute for Advanced Study, 1 Einstein Drive, Princeton, NJ 08540, USA*

(Dated: January 16, 2026)

ABSTRACT

Observations of active galactic nuclei have revealed a correlation between millimeter luminosity, X-ray luminosity, and mass, suggesting the emission in each of these bands is powered by a common source. Starting with a set of five general relativistic magnetohydrodynamic simulations with dynamically important magnetic fields, we perform ray-tracing calculations to produce spectra including synchrotron emission, bremsstrahlung emission, and Compton scattering. Our models with similar Eddington ratios to the objects for which the relationship was inferred naturally reproduce observations without tuning. Our lower Eddington ratio models depart from this relationship, likely attributable to an observational bias against extremely low accretion rates. We find that inverse Compton scattering dominates the production of X-rays over bremsstrahlung radiation in almost all models, and in all models consistent with the observed correlation. We find only a modest spin dependence in this relationship. This study demonstrates that a compact, hot accretion flow with dynamically important magnetic fields can naturally explain observed millimeter and X-ray properties in low-luminosity active galactic nuclei. Future work should explore the impacts of non-thermal electron populations, weaker magnetic fields, and radiative cooling.

Keywords: Polarimetry – Supermassive black holes – Magnetohydrodynamical simulations — Radiative transfer simulations – Accretion

1. INTRODUCTION

Supermassive black holes are found at the centers of most massive galaxies, where they accrete gas and impart energy to their hosts (J. Kormendy & L. C. Ho 2013; T. M. Heckman & P. N. Best 2014). When accreting, these Active Galactic Nuclei (hereafter AGNs) can outshine their host galaxies across most of the electromagnetic spectrum (e.g., H. Netzer 2015; R. C. Hickox & D. M. Alexander 2018). The emission mechanisms responsible for the different parts of the spectral energy distribution (SED) spectra are imperfectly understood, and thus developing physically motivated models of AGN emission is essential for constraining the underlying accretion physics.

Corresponding author: Kratika Mazde
 kratika.mazde@iap.fr

One interesting observational constraint is the classic “fundamental plane” (hereafter FP), an empirical correlation between the supermassive black hole mass (M_{BH}), 5 GHz radio luminosity ($L_{5,\text{GHz}}$) and 2-10 keV X-ray luminosity ($L_{X,2-10\text{keV}}$) that extends over many orders of magnitude (S. Corbel et al. 2003; E. Gallo et al. 2003; A. Merloni et al. 2003; E. Körding et al. 2006; R. M. Plotkin et al. 2012; Y. Wang et al. 2024; Q.-C. Long et al. 2025). This has been proposed as evidence for scale-invariant coupling between radiatively inefficient accretion disks and compact jets, where X-ray emission originates from the inner hot disk and radio emission from compact jets, modulated by black hole mass (S. Markoff et al. 2003; H. Falcke et al. 2004a; R. P. Fender et al. 2004; K. Gürtekin et al. 2019).

More recently, similar correlations have been found between millimeter and X-ray wavelengths (E. Behar et al. 2015, 2018; T. Kawamuro et al. 2022; C. Ricci et al.

2023). By including mass, I. Ruffa et al. (2024) claimed a “Millimeter Fundamental Plane” (hereafter mmFP), a relationship between black hole masses M_{BH} , nuclear ($\ll 100$ pc) luminosities $L_{\nu,mm}$ and intrinsic X-ray luminosities $L_{X,2-10keV}$. Temporal correlations observed between the two bands suggest a common and compact emission region (R. D. Baldi et al. 2015; E. Behar et al. 2020; P.-O. Petrucci et al. 2023; E. Shablovinskaya et al. 2024; A. Jana et al. 2025).

In the millimeter, general relativistic magnetohydrodynamics (GRMHD) simulations have been remarkably successful at matching resolved observations of accretion flows by the Event Horizon Telescope (EHT), even when including only thermal electron distribution functions (Event Horizon Telescope Collaboration et al. 2019a, 2021, 2022a, 2023, 2024a). Comparable models for radio jets require large simulation domains, often ad-hoc prescriptions for non-thermal electron distributions, and may be affected more strongly by environmental interactions (M. Mościbrodzka et al. 2016; G. E. Romero et al. 2017; R. Blandford et al. 2019). Consequently, the mmFP may be less affected by uncertain jet and plasma astrophysics and may probe smaller scales compared to the traditional fundamental plane using 5 GHz, making them more accessible to GRMHD modeling.

In modeling emission in these bands, the three most important radiative processes to consider are synchrotron emission (dominant in the radio/millimeter), and both bremsstrahlung and inverse-Compton scattering (which contribute to the X-rays). S. del Palacio et al. (2025) develop a one-zone corona emission model with a hybrid thermal and non-thermal electron population (Y. Inoue et al. 2019) and fit the spectral energy distributions (SEDs) of 7 radio-quiet AGNs. Their modeling infers for the corona modest non-thermal energy density fractions (0.5-10%), magnetic field strengths of 10-60 G, and radii of 60-250 gravitational radii. Meanwhile, A. Hankla et al. (2025) propose that millimeter emission in radio-quiet AGNs arises from an extended outflow around $\sim 10^4$ gravitational radii, preferring larger magnetic field strengths of $\sim 10^{3-4}$ G.

In this work, we investigate the mmFP by calculating SEDs using GRMHD simulations applicable to low-luminosity AGN for the first time. In section 2, we introduce the accretion flow simulations used in this study and the spectral modeling performed in this work. In section 3 we present the results of this study, spectral energy distributions from the millimeter to the X-ray across a grid of accretion flow parameters. We discuss the implications and limitations of our study in section 4, and summarize our conclusions in section 5.

2. METHODOLOGY

Starting with 5 “Magnetically Arrested Disk” (MAD) GRMHD simulations, we calculate SEDs as a function of SMBH mass M_{\bullet} , accretion rate \dot{m} , spin a_{\bullet} , and asymptotic ion-to-electron temperature R_{high} .

2.1. GRMHD Simulations

We use as our starting point the 3D GRMHD simulations described in V. Dhruv et al. (2025), which feature 5 spins, $a_{\bullet} \in \{-0.94, -0.50, 0.00, +0.50, +0.94\}$. These simulations have been well-studied in EHT theory analysis (Event Horizon Telescope Collaboration et al. 2022a, 2024a). To limit the scope of our analysis, we only include “Magnetically Arrested Disk” (MAD) simulations, which are characterized by dynamically important magnetic fields that alter the structure of the inflow and can power efficient jets (G. S. Bisnovatyi-Kogan & A. A. Ruzmaikin 1974; I. V. Igumenshchev et al. 2003; R. Narayan et al. 2003; A. Tchekhovskoy et al. 2011). When breaking degeneracies with either polarization or multi-wavelength information, EHT studies of M87* and Sgr A* (Event Horizon Telescope Collaboration et al. 2021, 2022a, 2023, 2024a) favor MAD models over less strongly magnetized “Standard and Normal Evolution” (SANE) models. Testing MAD models against the mmFP, derived from a more representative sample than the two EHT targets, is major motivation of this study.

The simulations were run using the KHARMA code (B. S. Prather 2024) and were initialized with a L. G. Fishbone & V. Moncrief (1976) torus of plasma with a pressure maximum at $41 r_g$ ⁶, threaded with an initially weak poloidal magnetic field. The resolution of these simulations is 288x128x128 in the radial, latitudinal, and azimuthal directions, and they are evolved to 30,000 t_g assuming an adiabatic index of 4/3. In this work, we select 21 snapshots from each of these simulations evenly spaced in time between 15,000 t_g and 30,000 t_g to ensure a sampling over quasi-steady accretion. In the following analysis, these snapshots are each individually rescaled to different masses and accretion rates.

2.2. SED Calculations

Following the PATOKA pipeline (G. N. Wong et al. 2022), we compute multi-wavelength spectra with the general relativistic Monte Carlo radiative transfer code grmonty (J. C. Dolence et al. 2009), which is optimized for optically thin, hot plasma in strong gravitational

⁶ We define $r_g = GM_{\bullet}/c^2$, where G is the gravitational constant, M_{\bullet} is the black hole mass, and c is the speed of light. We further define $t_g = r_g/c$.

fields. `grmonty` tracks photon emission, absorption, and scattering within the Kerr metric. The code includes synchrotron and bremsstrahlung emission as seed processes, and accounts for inverse Compton scattering in both the Thomson and Klein-Nishina regimes.

Emission is calculated in `grmonty` by discretizing the photon field into “superphotons” or “photon packets” generated with weight w , coordinates x^u , and wave vector k^u , in local orthonormal tetrads co-moving with the fluid. In a given time step Δt , superphotons over the whole volume of the model are produced according to

$$N_{s,tot} = \Delta t \int \sqrt{-g} dx d\nu d\Omega \frac{1}{w} \frac{j_\nu}{h\nu},$$

where j_ν is the fluid-frame emissivity, ν is the frequency, Ω is the solid angle in the fluid frame, and h is the Planck’s constant. To calculate ν and direction vectors \hat{n} , `grmonty` makes use of rejection sampling based on the local emissivity function. Emissivity modules are modular, allowing for different emission processes to be incorporated with minimal structural change. We use radiative transfer coefficients appropriate for thermal electron distribution functions.

Simulations are post-processed under the “fast light” approximation, enabling rapid calculation of spectra for each snapshot. Photons are produced as synchrotron or bremsstrahlung radiation, and they may be scattered as they move along their geodesics. This results in the production of inverse Compton upscattered photons. As we shall explore, synchrotron emission dominates in the radio to sub-millimeter, while inverse Compton upscattering produces high-energy tails relevant for X-ray observational constraints. The resulting SEDs serve as direct inputs for comparison with sub-millimeter and X-ray observations and allow for parameter estimation via forward modeling.

Parameter	Values
a_\bullet	-0.94, -0.5, 0, 0.5, 0.94
$M_\bullet [M_\odot]$	$10^6, 10^7, 10^8, 10^9, 10^{10}$
\dot{m}	$10^{-8}, 10^{-7}, 10^{-6}, 10^{-5}, 10^{-4}$
R_{high}	1, 40, 160

Table 1. Summary of models calculated in this work. All models are MAD and contain only thermal electron distribution functions. Each parameter combination is simulated 21 times to sample variability. Models with $\dot{m} = 10^{-4}$ were found to almost always exhibit unphysically large radiative efficiencies and are therefore excluded from most of our analysis.

Our GRMHD simulations span 5 spin values, and we rescale them in post-processing to explore three more

free parameters: SMBH mass (M_\bullet), Eddington ratio (\dot{m}), and asymptotic ion-to-electron temperature ratios in weakly magnetized regions (R_{high}). Our parameter combinations are summarized in Table 1. In our conventions, we define the Eddington ratio \dot{m} via

$$\dot{m} = \frac{\dot{M}_\bullet}{\dot{M}_{\text{Edd}}}, \quad (1)$$

where

$$\dot{M}_{\text{Edd}} = \frac{L_{\text{Edd}}}{0.1c^2} = \frac{4\pi GM_\bullet m_p}{0.1\sigma_T c}, \quad (2)$$

m_p is the mass of the proton, and σ_T is the electron cross-section to Thomson scattering. In other words, \dot{m} is the accretion rate relative to that of an Eddington-limited system converting mass to radiation with a fiducial 10% efficiency. True radiative efficiencies of a subset of our models obtained by integrating our spectra are presented and discussed in Appendix A.

The parameter R_{high} modulates the asymptotic ion-to-electron temperature ratio in each cell via

$$\frac{T_i}{T_e} = R_{\text{high}} \frac{\beta_p^2}{1 + \beta_p^2} + \frac{1}{1 + \beta_p^2} \quad (3)$$

where T_i and T_e are the ion and electron temperatures respectively, and β_p is the ratio of gas to magnetic pressure. This parameterization from M. Mościbrodzka et al. (2016) qualitatively captures the behavior of simulations where electron heating and cooling is modeled self-consistently. Heat is preferentially supplied to protons and electrons can more efficiently cool, leading to this temperature asymmetry, which is more pronounced in more weakly magnetized regions (M. J. Rees et al. 1982; R. Narayan & I. Yi 1995; E. Quataert & A. Gruzinov 1999; G. G. Howes 2010; Y. Kawazura et al. 2019; A. Chael et al. 2019; I. K. Dihingia et al. 2023). EHT studies have preferred $R_{\text{high}} \gg 1$ when accounting for both multi-wavelength and polarization constraints (Event Horizon Telescope Collaboration et al. 2021, 2022a, 2023, 2024a).

These four parameters—spin, mass, accretion rate, and asymptotic ion-to-electron temperature—define a physically motivated 4-dimensional parameter space over which our SEDs are computed. We sample 21 independent snapshots for each parameter combination to probe AGN variability and compute time averages. A minority of snapshots are discarded due to numerical artifacts in the radiative post-processing, identified through visual inspection.

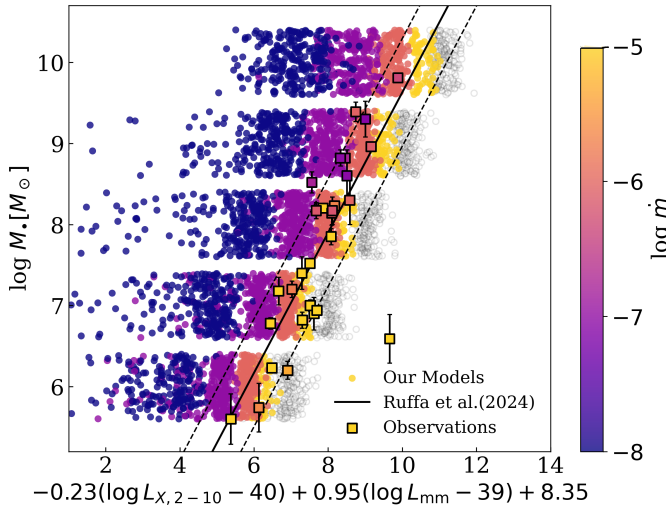


Figure 1. Comparison of our models with the “Millimeter Fundamental Plane” reported in [I. Ruffa et al. \(2024\)](#). Each point represents one GRMHD simulation, color-coded by \dot{m} . The best fit from [I. Ruffa et al. \(2024\)](#) is visualized with black lines, as well as the values from their primary sample of AGN. We find that our GRMHD models with $\log \dot{m} \lesssim -7$ drift to the left of the relation. Models with $\dot{m} = 10^{-4}$, shown here as gray circles, were almost all found to have $\epsilon_{\text{rad}} \gg 0.1$; these are excluded from future analysis.

3. RESULTS

3.1. Comparison with the *mmFP*

In Figure 1, we visualize our models on the millimeter fundamental plane proposed by [I. Ruffa et al. \(2024\)](#). Note that for plotting, we have artificially added scatter to the black hole masses of our simulations (sampled discretely at the 5 values listed in [Table 1](#)) to improve readability. Models are color-coded according to \dot{m} . In gray, we show our $\dot{m} = 10^{-4}$ models, which almost all exhibit $\epsilon \gg 0.1$ and are excluded from future figures. $L_{X,2-10}$ is obtained by integrating the specific luminosity L_ν between 2 and 10 keV, while we define $L_{\text{mm}} = \nu L_{\nu,\text{mm}}$. The relation found in [I. Ruffa et al. \(2024\)](#) is overplotted, including the primary sample of SMBHs used for this regression.⁷

We find that our models with $10^{-6} \leq \dot{m} \leq 10^{-5}$ are consistent with the relation, but models with lower \dot{m} drift to the left increasingly quickly as \dot{m} decreases. As we will explain in [subsubsection 3.2.1](#), we attribute this behavior in our models to an optical depth effect that only occurs when the peak frequency moves to lower frequencies than the millimeter. Our $\dot{m} = 10^{-4}$ models overshoot the relation to the right, and appear to

imply that AGN with larger Eddington ratios would become increasingly inconsistent with the mmFP. However, we find that the $\dot{m} = 10^{-4}$ models are radiatively efficient due to inverse Compton scattering. We expect that models that self-consistently account for the resultant cooling would attain significantly lower the temperatures at these accretion rates and higher, and thus the position of these models on the plot is unreliable.

3.2. Physical Drivers of the Fundamental Plane

In Figure 2, we plot the evolution of synchrotron, Inverse Compton, and bremsstrahlung emission among our time-averaged SED models as a function of M_\bullet , \dot{m} , and R_{high} . For this and subsequent figures, we normalize our spectra by the bolometric luminosity, L_{bol} , which is dominated by the synchrotron peak in our models. ALMA band 6 is demarcated with a gray column, while the 2-10 keV X-ray band is demarcated with a blue column. We fix $a_\bullet = 0.94$ and show two masses, $10^9 M_\odot$ in the top row, and $10^6 M_\odot$ in the bottom row.

Here, we will break down the emission mechanisms and parameter dependencies in each band. In interpreting these results, it is important to bear in mind the following scalings. The density in GRMHD simulations scales as

$$n \propto \dot{m} M_{\bullet}^{-1}, \quad (4)$$

the magnetic field strength scales as

$$B \propto n^{1/2} \propto \dot{m}^{1/2} M_{\bullet}^{-1/2}, \quad (5)$$

and T_e evolves according to [Equation 3](#), which behaves as

$$T_e \propto \begin{cases} R_{\text{high}}^{-1}, & \text{for } \beta \gg 1 \\ R_{\text{high}}^0, & \text{for } \beta \ll 1 \end{cases} \quad (6)$$

without a dependence on \dot{m} or M_\bullet . Any dependence on a_\bullet is indirect, through emergent evolution in n , B , and T_e .

3.2.1. Millimeter: Sourced by Synchrotron

Shown in the leftmost column of Figure 2, synchrotron emission dominates the millimeter band for all of our models. The turnover frequency increases as \dot{m} increases, decreases as R_{high} increases, and increases as M_{\bullet} increases. All of these behaviors can be understood through the scaling of the critical frequency for synchrotron emission, which follows

⁷ These include the WISDOM and literature sources tabulated in their Table A1, but not the extended BASS sample.

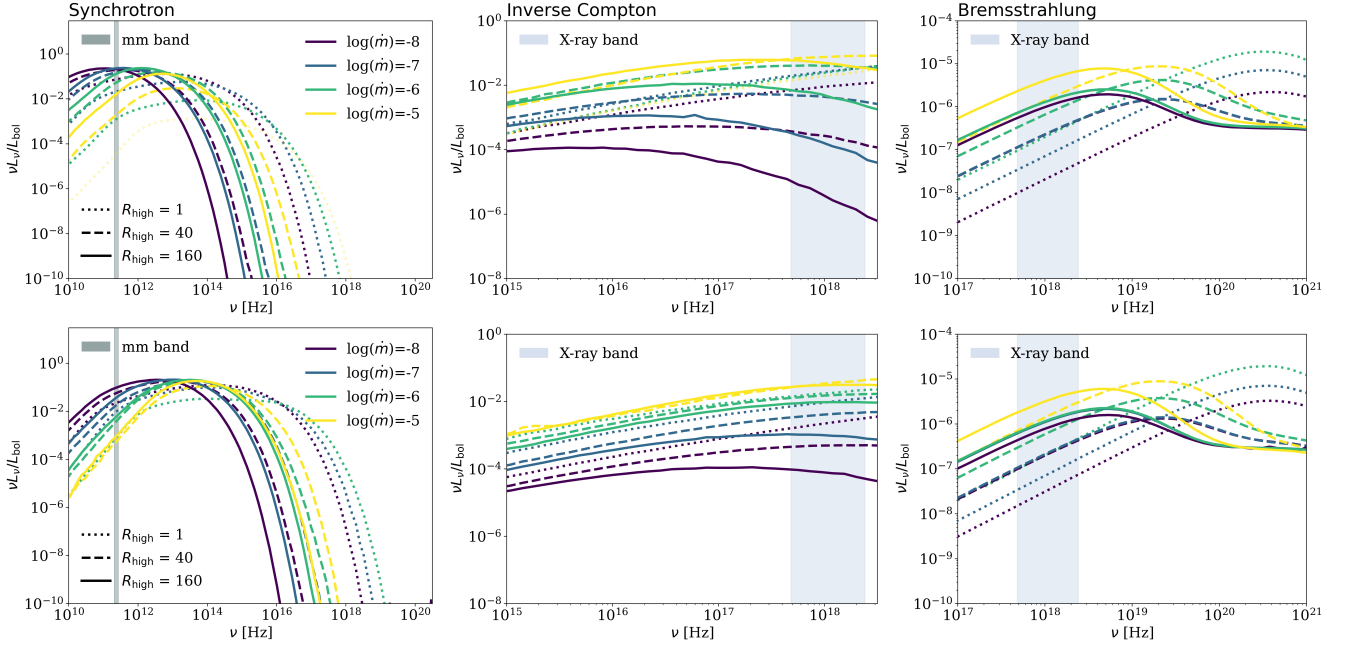


Figure 2. Spectral energy distributions as a function of Eddington ratio \dot{m} and R_{high} with fixed spin, $a_{\bullet}=+0.94$. Models with $M_{\text{BH}}=10^9 M_{\odot}$ are shown in the top row, and models with $M_{\text{BH}}=10^6 M_{\odot}$ are shown in bottom row.

$$\nu_{\text{synch}} \propto T_e^2 B \propto T_e^2 \dot{m}^{1/2} M_{\bullet}^{-1/2} \quad (7)$$

using Equation 5. At lower frequencies, these spectra follow the Rayleigh-Jeans law $L_{\nu} \propto \nu^2$ since we use a thermal eDF, while power-law eDFs would exhibit $L_{\nu} \propto \nu^{5/2}$. At higher frequencies, these spectra inherit the exponential cutoff of the thermal eDF, which would fall off more gently if we had considered non-thermal electrons (F. Özel et al. 2000; A. Ricarte et al. 2023). In the optically thin limit, the total power emitted by synchrotron radiation follows $L \propto nB^2V$, where $V \propto M_{\bullet}^3$ is the volume of the emitting region. Following our scalings, we can expect $L \propto \dot{m}^2 M_{\bullet}$. This strong scaling with \dot{m} explains the clear \dot{m} dependence in Figure 1, but may seem at odds with the I. Ruffa et al. (2024) sample, where they report L_{mm} mostly encodes M_{\bullet} . This can be explained if for the objects in this sample, typically $\nu_{\text{synch}} \gtrsim 230$ GHz. In this case, the emission transitions to optically thick at this frequency, and L_{mm} begins to scale with the radius R of the 230 GHz photosphere. For an optically thick ball of gas, $L_{\text{mm}} \propto R^2 \propto M_{\bullet}^2$, but the actual scaling would depend in detail on the radial profiles of n , B , and T_e . We discuss how we expect the mmFP to break down at low \dot{m} in Appendix B.

3.2.2. X-ray: Dominated by Inverse Compton

In the second and third columns of Figure 2 we plot the Inverse Compton “IC” and bremsstrahlung components of the spectrum respectively. IC clearly dominates the X-ray emission in *all* of our models, even

for $M_{\bullet}=10^6 M_{\odot}$ and $\dot{m}=10^{-8}$. For some of our $\dot{m}=10^{-5}$ models, the total IC luminosity becomes comparable to synchrotron. All of our models are in the single-scattering regime, and the typical IC photon will be up-scattered to frequency $\nu_{\text{IC}} \approx \frac{4}{3}\langle\gamma^2\rangle\nu_{\text{seed}}$, where $\gamma^2 \propto T_e^2$. The seed photons come from synchrotron, and thus ν_{IC} inherits the scaling of $\nu_{\text{synch}} \propto T_e^2 B$. As a result,

$$\nu_{\text{IC}} \propto T_e^4 \dot{m}^{1/2} M_{\bullet}^{-1/2}. \quad (8)$$

This makes the X-ray part of the spectrum extremely sensitive to R_{high} . When these models were considered in Event Horizon Telescope Collaboration et al. (2022a), an upper limit on the X-ray emission of Sgr A* led to a preference for larger values of R_{high} , consistent with these findings. The large R_{high} may itself be a consequence of electron cooling due to IC scattering.

The other intrinsic source of emission in our simulations is bremsstrahlung, or “free-free” emission. Unlike synchrotron emission, bremsstrahlung is insensitive to the magnetic field. The third column demonstrates that for almost all of our models, bremsstrahlung contributes negligibly to the bolometric luminosity of the system, although it is worth exploring physical trends. Here, emission peaks at $\nu_{\text{brems}} \sim k_B T_e/h \sim 10^{20}$ Hz, in the gamma rays for $T_e \sim 1$. As R_{high} increases, the single broad peak splits into two. We suspect that the R_{high} prescription splits the accretion flow into a $T_e \sim 1$ jet funnel component and a $T_e \sim 1/R_{\text{high}}$ disk component.

Bremsstrahlung has been shown to dominate the X-ray emission in other GRMHD models, particularly SANEs (R. Yarza et al. 2020; Event Horizon Telescope Collaboration et al. 2022a, 2024b). This is expected as SANE models often have larger values of \dot{m} by orders of magnitude and lower values of T_e by around an order of magnitude, and

$$j_{\nu, \text{bremss}} \propto n^2 T_e^{-1/2} \propto \dot{m}^2 M_{\bullet}^{-2} T_e^{-1/2}. \quad (9)$$

The scaling of the IC luminosity with accretion rate can be understood in the context of hot accretion flow models. In the optically thin, single-scattering regime relevant for our models, the inverse Compton luminosity is given by

$$L_{\text{IC}} \simeq y L_{\text{syn}}, \quad (10)$$

where $y = 4\Theta_e \max(\tau, \tau^2)$ is the Compton y -parameter, and Θ_e is the electron temperature in units of electron rest mass energy. Since the Thomson optical depth scales as $\tau \propto n_e \propto \dot{m}$, $y \propto \dot{m}$. Taken together, these scalings yield $L_{\text{IC}} \propto \dot{m}^3$ (see also F. Yuan et al. 2003b; F. Yuan & R. Narayan 2014). This steeper scaling with \dot{m} compared to Bremsstrahlung implies that Bremsstrahlung dominates X-ray emission at the lowest \dot{m} values.

3.3. Only a Modest Dependence on Spin

The classic fundamental plane, where radio emission plays the role of millimeter emission, is most strongly established for radio-loud AGN (H. Falcke et al. 2004b; K. Gültekin et al. 2019). Radio emission originating from a jet may attain its energy through the R. D. Blandford & R. L. Znajek (1977) mechanism, wherein the jet efficiency follows $\eta_{\text{jet}} \propto a_{\bullet}^2 B^2$. A spread in the spins of the SMBH population is proposed as an explanation for variations in radio-loudness (M. Volonteri et al. 2007), as is a spread in magnetic field strengths (M. Sikora & M. C. Begelman 2013).

Fixing $R_{\text{high}} = 40$, we plot our total SEDs as a function of M_{\bullet} , \dot{m} , and a_{\bullet} in Figure 3. We would expect millimeter emission sourced by R. D. Blandford & R. L. Znajek (1977) jet power to exhibit a similarly strong dependence on a_{\bullet} . Instead, we find only a modest dependence on spin, generally consistent with EHT studies using these models (Event Horizon Telescope Collaboration et al. 2022a). The most pronounced spin evolution occurs between spins 0.5 and 0.94. These $a_{\bullet} = 0.94$ models exhibit hotter jet funnels (see Fig. 7 of V. Dhruv et al. 2025) than their lower spin counterparts, to which we attribute the higher synchrotron frequencies and IC normalizations.

3.4. Which models lie on the relation?

In Figure 4, we select the snapshots consistent with the mmFP across R_{high} , \dot{m} , spin, and $\log(L_{\text{IC}}/L_{\text{bremss}})$, where $L_{\text{IC}}/L_{\text{bremss}}$ is the ratio of Inverse Compton luminosity to bremsstrahlung luminosity only considering 2 to 10 keV emission. As discussed in subsection 3.2, models with smaller \dot{m} systematically depart from the relation. All snapshots which satisfy the mmFP have $L_{\text{IC}}/L_{\text{bremss}} > 1$, and only 0.7% of the total snapshots have $L_{\text{IC}}/L_{\text{bremss}} < 1$. This is consistent with our discussion in subsubsection 3.2.2.

We notice a preference for larger R_{high} among mmFP-consistent models, which in the aggregate of models is driven by $\dot{m} = 10^{-7}$. Larger \dot{m} models typically fall within the scatter regardless of R_{high} . Because $\nu_{\text{synch}} \propto T_e^2 B$ and $\nu_{\text{IC}} \propto T_e^4 \dot{m}^{1/2} M_{\bullet}^{-1/2}$, increasing R_{high} suppresses the X-rays relative to the millimeter. This helps “tune” the intrinsic X-rays into the observed regime without requiring jets or non-thermal electrons, and is consistent with EHT studies that favor large R_{high} to satisfy X-ray upper limits (Event Horizon Telescope Collaboration et al. 2022a).

4. DISCUSSION

We have computed a grid of SEDs from GRMHD models spanning four parameters, M_{\bullet} , \dot{m} , a_{\bullet} , and R_{high} . Here, we summarize the effects of each of these parameters in our models.

- The black hole mass M_{\bullet} affects the emitting volume and the scalings of the density and magnetic field. At fixed Eddington ratios, increasing M_{\bullet} lowers the density ($n \propto \dot{m} M_{\bullet}^{-1}$), and magnetic field ($B \propto n^{1/2}$), which results in lower synchrotron emissivity per unit volume. However, the total emitting volume grows rapidly ($V \propto M_{\bullet}^3$) and this more than compensates, resulting in a net scaling of $L_{\nu, \text{mm}} \propto \dot{m}^2 M_{\bullet}$. The X-ray luminosity scales more steeply, as $L_{\nu, \text{mm}} \propto \dot{m}^{2+\alpha} M_{\bullet}$ with $\alpha > 0$, reflecting the additional dependence on inverse-Compton scattering and electron temperature T_e .
- Spin a_{\bullet} has only a modest influence on our spectra. The main effect of increasing spin is through the temperature dependence, where higher spins have hotter accretion flows, and progrades are hotter than retrogrades (V. Dhruv et al. 2025). Models with higher spins, and therefore hotter plasma, have higher synchrotron frequencies and more inverse Compton scattering.
- The Eddington ratio \dot{m} increases the bolometric luminosity via $L_{\text{bol}} \propto \dot{m}^2$, and the IC contribu-

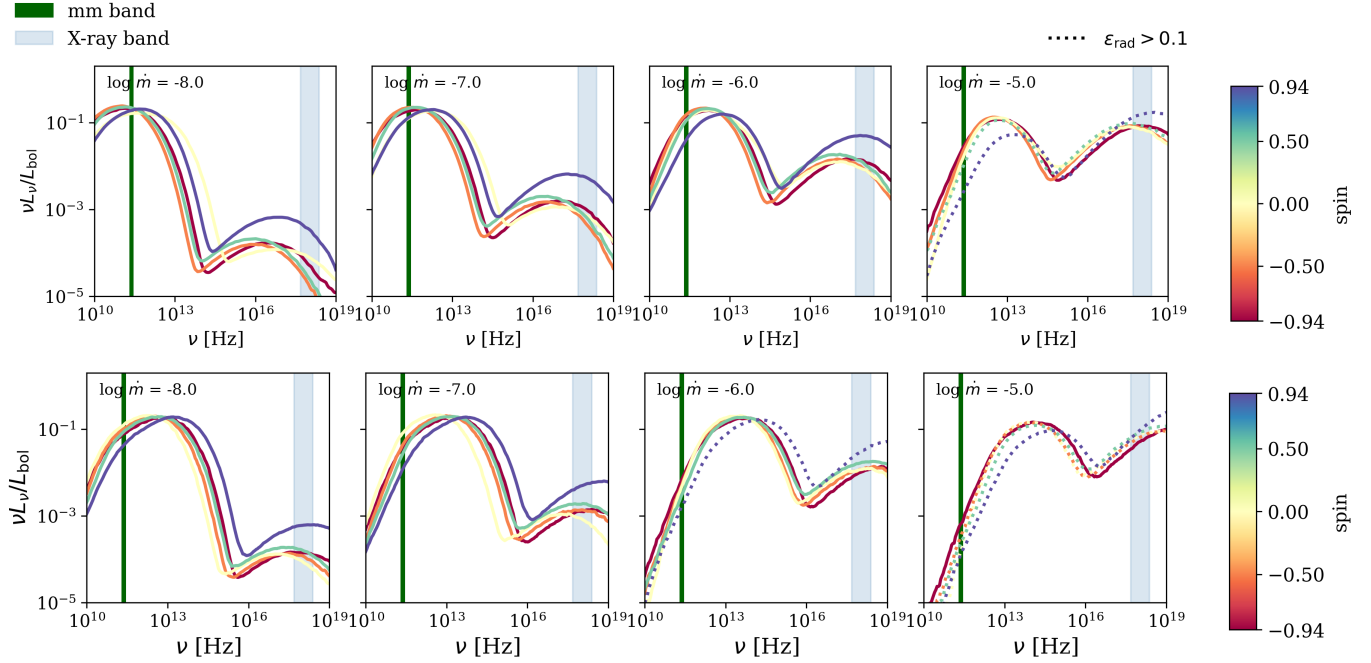


Figure 3. A grid of time-averaged normalized total spectra as a function of two parameters, Eddington ratio \dot{m} , spin a_\bullet , with fixed $R_{high} = 40$. Models with $M_{BH} = 10^9 M_\odot$ are shown in the top row, and models with $M_{BH} = 10^6 M_\odot$ are shown in bottom row respectively.

tion increases even more steeply via $L_{IC} \propto \dot{m}^3$ in the optically thin regime (R. Narayan et al. 1995). With increasing \dot{m} , density and magnetic field strength increases, which in turn pushes the synchrotron and IC peaks to higher frequencies and boosts the overall bolometric luminosity. I. Ruffa et al. (2024) reports that L_{mm} is more sensitive to M_\bullet than \dot{m} , while we see that models with $\dot{m} < 10^{-6}$ drift to the left of the mmFP. This can be understood as a photosphere effect: for sufficiently large \dot{m} , the turnover frequency occurs near or higher than the millimeter. The total luminosity therefore scales more with the size of the emitting region than with the accretion rate, with the exact scaling dependent on the details of the n , B , and T_e profiles.

- Models with larger R_{high} have lower electron temperatures in the disk by construction. Increasing R_{high} therefore decreases the synchrotron and IC power, and moves spectral peaks to lower frequencies. The X-ray component of the spectra is particularly sensitive to this parameter in that $\nu_{IC} \propto T_e^{-4}$. Event Horizon Telescope Collaboration et al. (2022a) reported that models with larger R_{high} could more comfortably pass X-ray upper limits, which can be understood in the context of this strong temperature scaling.

We now discuss some physical limitations of this work. All models in this study assume thermal electron distributions. However, non-thermal electron populations, especially in jet or shock associated regions, could produce a high-energy tail of electron energies. So far, ideal GRMHD simulations have been remarkably successful models for explaining the low Eddington ratio systems of Sgr A* and M87*, and physically motivated non-thermal electron prescriptions tend to produce only slight differences (Event Horizon Telescope Collaboration et al. 2022a). Interestingly, Event Horizon Telescope Collaboration et al. (2022a) found that including non-thermal electrons increased the failure rate of models due to the X-ray constraint: adding high-energy electrons can easily result in excessive IC, since $\nu_{IC} \approx \langle \gamma^2 \rangle \nu_{seed}$. As a result, we speculate that including a significant non-thermal electron component would systematically worsen agreement with the mmFP.

While jets are present in our simulations, their effect is minimized due to our thermal eDF assumption. Classical fundamental plane models (S. Heinz & R. A. Sunyaev 2003; F. Yuan et al. 2003a; W. Cui & F. Yuan 2005) suggest radio and X-ray emission correspond to jet synchrotron and synchrotron self-Compton processes. However, our work illustrates that extended jet emission is not required to reproduce mmFP, at least within the parameter space explored in this study. Adding extended jet emission in the millimeter would systematically shift

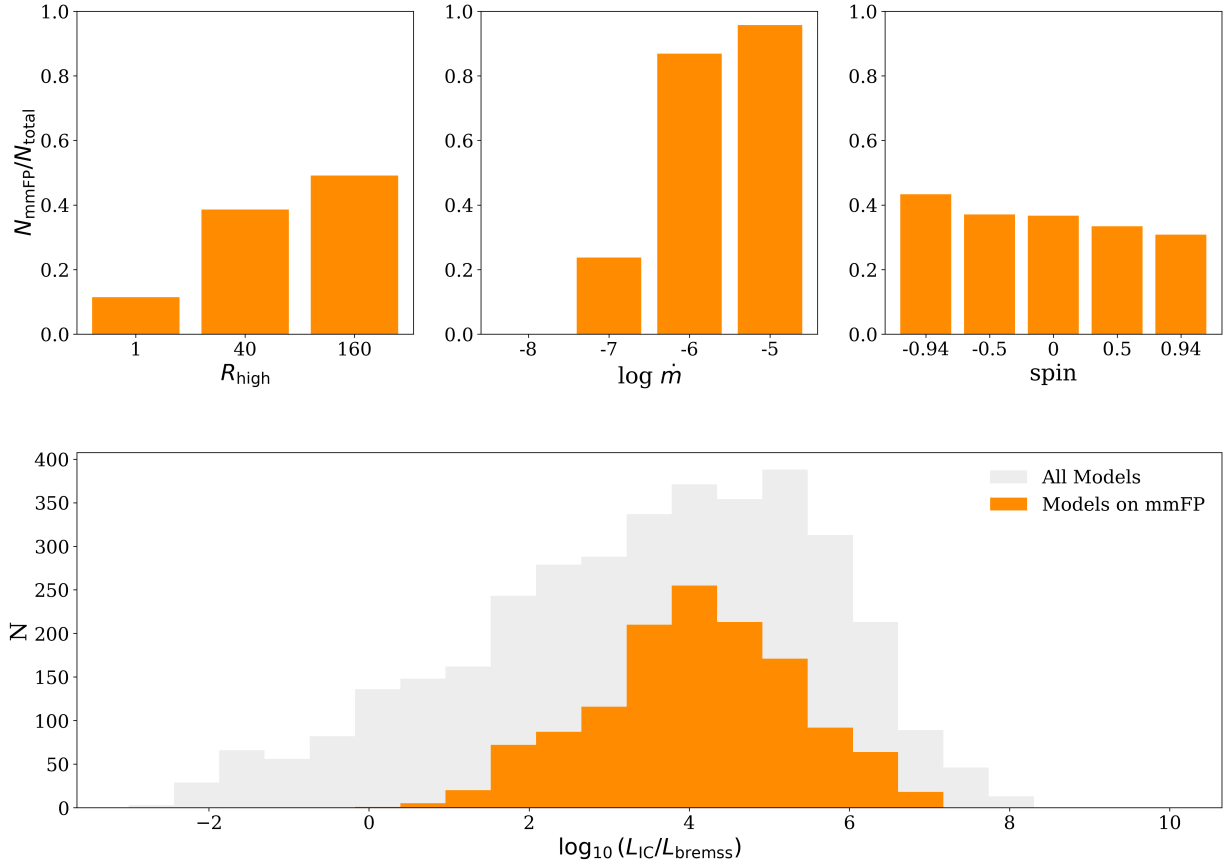


Figure 4. Top: Fraction of model snapshots which satisfy mmFP as a function of R_{high} , Eddington ratio \dot{m} and spin. Bottom: Distribution of $\log(L_{\text{IC}}/L_{\text{bremss}})$ for all models in grey, compared to those consistent with the mmFP in orange.

objects to the right of this relation, if it does not come with the right amount of X-ray emission to cancel this effect. Size constraints with high enough resolution to distinguish jet from disk would therefore be useful for continuing to probe the physical origins of the mmFP. For Sgr A*, the EHT constrains no less than 83% of the observed emission to come from the compact ring (Event Horizon Telescope Collaboration et al. 2022b), while for M87* the compact flux and jet components are comparable (Event Horizon Telescope Collaboration et al. 2019b). Extending the EHT array into space with missions such as the Black Hole Explorer (BHEX) will enable horizon-scale images of an additional ~ 10 objects that lie on the mmFP (X. A. Zhang et al. 2025). Such size constraints will help discriminate this model from others where the millimeter emission originates from much larger radii (A. Hankla et al. 2025).

Our work neglects radiative cooling, which is expected to affect the temperature for Eddington ratios as small as $\dot{m} \gtrsim 10^{-7}$ (S. Dibi et al. 2012) and the global dynamics for Eddington ratios $\dot{m} \gtrsim 10^{-5.5}$ (A. Singh et al. 2025). Indeed, this latter value roughly matches the transition where our models begin to produce unac-

ceptably high radiative efficiencies due to IC scattering. Modulating R_{high} allows us to capture the first set of effects to some extent, and we speculate that including radiative cooling should have similar effects as R_{high} . Interestingly, radiative GRMHD simulations tend not to produce low enough temperatures (large enough effective values of R_{high}) to reproduce observations, an area of ongoing development in the field (e.g., I. K. Dihingia et al. 2023; A. Chael 2025).

We performed a series of tests on a snapshot with $a_{\bullet} = 0.94$, $R_{\text{high}} = 40$, $M_{\bullet} = 10^9 M_{\odot}$ and $\dot{m} = 10^{-4}$ to assess the impact of several numerical limitations: the magnetization ceiling, the temperature floor, and the finite domain size. First, we applied a “sigma cut” by zeroing the density in all cells with plasma $\sigma > 1$. Second, our implementation of `grmonty` sets a temperature floor of $\Theta_e = 10^{-3}$, and we assessed the sensitivity to the electron temperature floor (to any cool, non-relativistic electron populations) by increasing it to 0.3. Third, we tested the impact of the outer torus in the initial conditions by zeroing the density in cells with $r > 100 r_g$. None of these tests resulted in notable changes to the SED in the bands considered.

5. CONCLUSION

In this work, we tested a four-dimensional grid of compact, hot accretion flow models with dynamically important magnetic fields against the Millimeter Fundamental Plane (mmFP) of [I. Ruffa et al. \(2024\)](#), an observed correlation between millimeter luminosity, X-ray luminosity and SMBH mass. Our main results are as follows:

- Models with $\dot{m} \gtrsim 10^{-6}$ naturally reproduce the mmFP without any fine-tuning. As \dot{m} decreases below the values exhibited by AGN in the [I. Ruffa et al. \(2024\)](#) sample, models drift leftward of the relationship.
- X-rays are generated by inverse Compton scattering in all of our time-averaged models. This Compton-produced component exceeds direct bremsstrahlung emission even for models with $\dot{m} = 10^{-8}$.
- We explore trends in our models as a function of model parameters. Spin has only a minor effect on the luminosity in either band, due to higher temperatures achieved with higher spins. Cooling electrons (with the parameter R_{high}) has a significant effect on both bands, especially the amount of X-rays produced by IC scattering.

We conclude that compact, hot accretion flows with dynamically important magnetic fields naturally reproduce the mmFP. This work yields two testable predictions:

1. Objects with $\dot{m} < 10^{-7}$ should systematically migrate to the left of the mmFP. We confirm this behavior in the case of Sgr A*.
2. High-resolution size constraints, such as those enabled by EHT and BHEX, should localize the millimeter emitting region to scales of $\lesssim 10 - 100 GM_{\bullet}/c^2$ for the Eddington ratios of interest.

Our investigation is restricted to $\dot{m} \lesssim 10^{-5}$ due to the lack of radiative cooling in these models. Future investigation into the impact of weaker magnetic fields, non-thermal electrons, and radiative cooling would help determine the generality of the conclusions reached in this work.

6. ACKNOWLEDGMENTS

The authors thank Michael D. Johnson and Daniel Palumbo for informative discussions. The authors also thank Charles Gammie and Vedant Dhruv for making the GRMHD simulations used in this work publicly available.

This publication is funded in part by the Gordon and Betty Moore Foundation, Grant GBMF-12987. This publication is supported by the Black Hole Initiative at Harvard University, which is funded by grants from the John Templeton Foundation (Grant #62286) and the Gordon and Betty Moore Foundation (Grant GBMF-8273)—although the opinions expressed in this work are those of the author(s) and do not necessarily reflect the views of these Foundations. K.M. was supported by École Doctorale 564 Physique en Île-de-France, and G.N.W. was supported by the Princeton Gravity Initiative and the Taplin Fellowship. K.M. was also supported in part through generous support from Mr. Michael Tuteur and Amy Tuteur, MD. The authors acknowledge financial support from the National Science Foundation (AST-2307887).

APPENDIX

A. RADIATIVE EFFICIENCIES

We define the radiative efficiency ϵ_{rad} as the fraction of rest-mass energy converted into radiation. For each of our models, we compute their radiative efficiencies by calculating

$$\epsilon_{\text{rad}} = \frac{L_{\text{bol}}}{\dot{M}_{\bullet}c^2}, \quad (\text{A1})$$

where $L_{\text{bol}} = \int L_{\nu}d\nu$ is the bolometric luminosity and $\dot{M}_{\bullet} = \dot{m}\dot{M}_{\text{Edd}}$ is the mass accretion rate. The results are tabulated in [Table 2](#). Our GRMHD simulations are meant to represent radiatively inefficient accretion flows and thus physically consistent models should have $\epsilon_{\text{rad}} \ll 1$. In our paper, we reject all models with $\epsilon_{\text{rad}} > 0.1$, which includes

all $\dot{m} = 10^{-4}$ models. We find that IC tends to dominate the SED in models with $\epsilon_{\text{rad}} > 0.1$; IC would therefore cool the plasma in a more physically complete model.

a_{\bullet}	$\log M_{\bullet}$	$\log \dot{m}$	R_{high}	$\log \epsilon_{\text{rad}}$	a_{\bullet}	$\log M_{\bullet}$	$\log \dot{m}$	R_{high}	$\log \epsilon_{\text{rad}}$
0.94	6	-5	160	-0.33	0	6	-5	160	-0.83
0.94	6	-6	160	-1.48	0	6	-6	160	-1.87
0.94	6	-7	160	-2.49	0	6	-7	160	-2.86
0.94	6	-8	160	-3.48	0	6	-8	160	-3.84
0.94	7	-5	160	-0.34	0	7	-5	160	-1.84
0.94	7	-6	160	-1.50	0	7	-6	160	-2.87
0.94	7	-7	160	-2.50	0	7	-7	160	-3.86
0.94	7	-8	160	-3.49	0	7	-8	160	-4.85
0.94	8	-5	160	-0.36	0	8	-5	160	-2.84
0.94	8	-6	160	-1.52	0	8	-6	160	-3.87
0.94	8	-7	160	-2.52	0	8	-7	160	-4.86
0.94	8	-8	160	-3.50	0	8	-8	160	-5.85
0.94	9	-5	160	-0.39	0	9	-5	160	-3.83
0.94	9	-6	160	-1.54	0	9	-6	160	-4.87
0.94	9	-7	160	-2.54	0	9	-7	160	-5.85
0.94	9	-8	160	-3.52	0	9	-8	160	-6.84

Table 2. Radiative efficiencies for a subset of our prograde ($a_{\bullet} = +0.94$) and nonspinning ($a_{\bullet} = 0$) GRMHD models.

B. OBSERVATIONAL SELECTION EFFECTS

In subsection 3.1, we found that models with $\dot{m} < 10^{-6}$ systematically drift to the left of the mmFP. In subsection 3.2.1, we argued that a strong dependence on \dot{m} is expected, but only when \dot{m} is sufficiently small that the synchrotron turnover frequency $\nu_{\text{synch}} < 230$ GHz. Here, we explore the possibility that an observational selection effect explains the difference between our models and the I. Ruffa et al. (2024) sample.

In Figure 5, we first compare our models with the I. Ruffa et al. (2024) sample in the $M_{\bullet} - L_{mm}$ plane. The I. Ruffa et al. (2024) sample spans a broad range in both M_{\bullet} and \dot{m} (inferred from L_x). Their \dot{m} values exhibit 0th, 25th, 50th, 75th, and 100th percentile values of -7.1, -6.0, -4.9, -3.1, and -1.1 respectively. All of their objects with $\dot{m} < 10^{-6}$ have $M_{\bullet} > 10^8 M_{\odot}$. We color-code both our models and the observational data points by \dot{m} , although in the case of the observational data, this is computed assuming $L_x = 0.1L_{\text{bol}}$ and $\dot{m} = L_{\text{bol}}/L_{\text{Edd}}$, which is not generally true in our models. Note that although our color bar saturates at $\dot{m} = 10^{-5}$, about half of the I. Ruffa et al. (2024) objects lie above that value. Comparing the models with the observed data, our models clearly extend to far smaller values of L_{mm} than the observed sample. At fixed L_{mm} and M_{\bullet} , the observations and models roughly agree on \dot{m} , implying that our models are producing reasonable millimeter luminosities, but the observed sample only overlaps with the upper envelope of our models.

The I. Ruffa et al. (2024) objects fall roughly above the dashed line defined by $\log L_{mm} [\text{erg s}^{-1}] = 35.5 + (\log M_{\bullet} [M_{\odot}] - 6)$. As shown in the second panel, if we select for the models that lie above this line, they agree very well with the mmFP. That is, if we select for models with comparable millimeter luminosities to the observed sample, then they naturally produce an appropriate amount of X-ray emission via IC scattering. This suggests that an observational selection effect leads to the disagreement of our low \dot{m} models with the mmFP. Indeed, when we include Sgr A* on these plots, with $L_x = 2.4 \times 10^{33} \text{ erg s}^{-1}$ (F. K. Baganoff et al. 2003), $M_{\bullet} = 4.14 \times 10^6 M_{\odot}$ (T. Do et al. 2019), $L_{mm} = 4.6 \times 10^{34} \text{ erg s}^{-1}$ (Event Horizon Telescope Collaboration et al. 2022c), and a “best bet” estimate of $\dot{m} \approx 10^{-7.2}$ (Event Horizon Telescope Collaboration et al. 2022a, 2024a), we find that it agrees well with our models but has much lower L_{mm} than the I. Ruffa et al. (2024) sample and falls to the left of this relationship as expected.

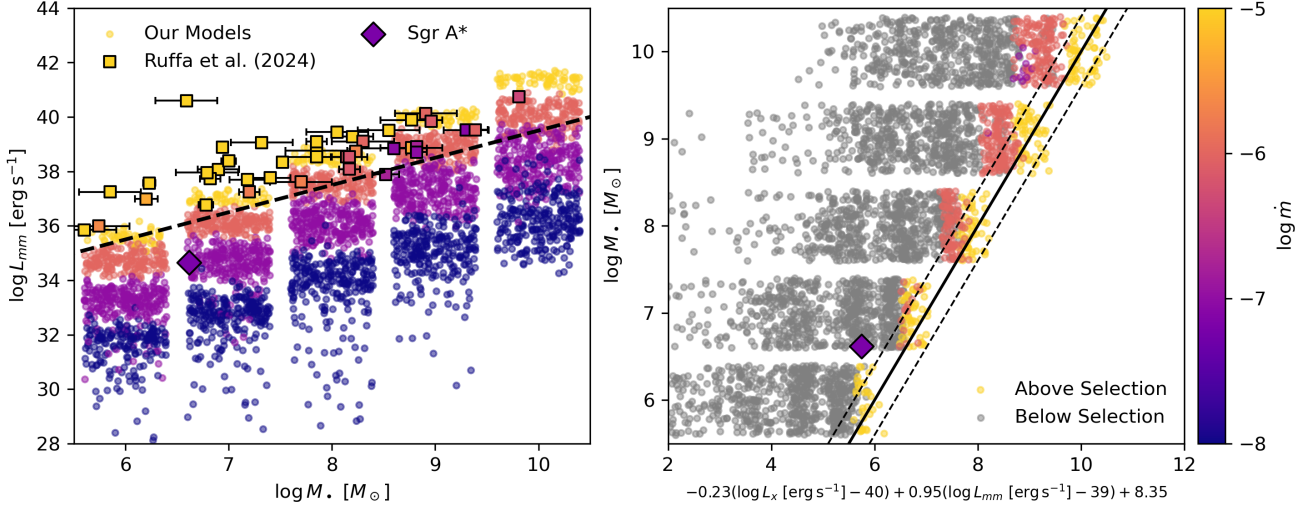


Figure 5. Proposed impact of selection effects. In the leftmost panel, we compare our GRMHD models to the observational sample from I. Ruffa et al. (2024), color-coded by \dot{m} . For a given L_{mm} and M_{\bullet} , the I. Ruffa et al. (2024) sample generally overlaps with our models in \dot{m} , suggesting that our models are producing reasonable millimeter luminosities. The I. Ruffa et al. (2024) sample only includes objects roughly above the dashed black line. If we restrict our models to those above this line, we find much better agreement with the mmFP in the right panel. This suggests that objects should drift to the left of the mmFP at lower accretion rates, as the synchrotron turnover frequency moves to lower frequencies.

A larger sample of extremely low Eddington ratio objects could therefore place interesting constraints on the physical origins of the mmFP.

REFERENCES

Baganoff, F. K., Maeda, Y., Morris, M., et al. 2003, ApJ, 591, 891, doi: [10.1086/375145](https://doi.org/10.1086/375145)

Baldi, R. D., Behar, E., Laor, A., & Horesh, A. 2015, MNRAS, 454, 4277, doi: [10.1093/mnras/stv2284](https://doi.org/10.1093/mnras/stv2284)

Behar, E., Baldi, R. D., Laor, A., et al. 2015, MNRAS, 451, 517, doi: [10.1093/mnras/stv988](https://doi.org/10.1093/mnras/stv988)

Behar, E., Vogel, S., Baldi, R. D., Smith, K. L., & Mushotzky, R. F. 2018, MNRAS, 478, 399, doi: [10.1093/mnras/sty850](https://doi.org/10.1093/mnras/sty850)

Behar, E., Kaspi, S., Paubert, G., et al. 2020, MNRAS, 491, 3523, doi: [10.1093/mnras/stz3273](https://doi.org/10.1093/mnras/stz3273)

Bisnovatyi-Kogan, G. S., & Ruzmaikin, A. A. 1974, Ap&SS, 28, 45, doi: [10.1007/BF00642237](https://doi.org/10.1007/BF00642237)

Blandford, R., Meier, D., & Readhead, A. 2019, ARA&A, 57, 467, doi: [10.1146/annurev-astro-081817-051948](https://doi.org/10.1146/annurev-astro-081817-051948)

Blandford, R. D., & Znajek, R. L. 1977, MNRAS, 179, 433, doi: [10.1093/mnras/179.3.433](https://doi.org/10.1093/mnras/179.3.433)

Chael, A. 2025, MNRAS, 537, 2496, doi: [10.1093/mnras/staf200](https://doi.org/10.1093/mnras/staf200)

Chael, A., Narayan, R., & Johnson, M. D. 2019, MNRAS, 486, 2873, doi: [10.1093/mnras/stz988](https://doi.org/10.1093/mnras/stz988)

Corbel, S., Nowak, M. A., Fender, R. P., Tzioumis, A. K., & Markoff, S. 2003, A&A, 400, 1007, doi: [10.1051/0004-6361:20030090](https://doi.org/10.1051/0004-6361:20030090)

Cui, W., & Yuan, F. 2005, in American Astronomical Society Meeting Abstracts, Vol. 207, American Astronomical Society Meeting Abstracts, 102.04

del Palacio, S., Yang, C., Aalto, S., et al. 2025, A&A, 701, A41, doi: [10.1051/0004-6361/202554936](https://doi.org/10.1051/0004-6361/202554936)

Dhruv, V., Prather, B., Wong, G. N., & Gammie, C. F. 2025, ApJS, 277, 16, doi: [10.3847/1538-4365/adaea6](https://doi.org/10.3847/1538-4365/adaea6)

Dibi, S., Drappeau, S., Fragile, P. C., Markoff, S., & Dexter, J. 2012, MNRAS, 426, 1928, doi: [10.1111/j.1365-2966.2012.21857.x](https://doi.org/10.1111/j.1365-2966.2012.21857.x)

Dihingia, I. K., Mizuno, Y., Fromm, C. M., & Rezzolla, L. 2023, MNRAS, 518, 405, doi: [10.1093/mnras/stac3165](https://doi.org/10.1093/mnras/stac3165)

Do, T., Hees, A., Ghez, A., et al. 2019, Science, 365, 664, doi: [10.1126/science.aav8137](https://doi.org/10.1126/science.aav8137)

Dolence, J. C., Gammie, C. F., Mościbrodzka, M., & Leung, P. K. 2009, ApJS, 184, 387, doi: [10.1088/0067-0049/184/2/387](https://doi.org/10.1088/0067-0049/184/2/387)

Event Horizon Telescope Collaboration, Akiyama, K., Alberdi, A., et al. 2019a, *ApJL*, 875, L5, doi: [10.3847/2041-8213/ab0f43](https://doi.org/10.3847/2041-8213/ab0f43)

Event Horizon Telescope Collaboration, Akiyama, K., Alberdi, A., et al. 2019b, *ApJL*, 875, L4, doi: [10.3847/2041-8213/ab0e85](https://doi.org/10.3847/2041-8213/ab0e85)

Event Horizon Telescope Collaboration, Akiyama, K., Algaba, J. C., et al. 2021, *ApJL*, 910, L13, doi: [10.3847/2041-8213/abe4de](https://doi.org/10.3847/2041-8213/abe4de)

Event Horizon Telescope Collaboration, Akiyama, K., Alberdi, A., et al. 2022a, *ApJL*, 930, L16, doi: [10.3847/2041-8213/ac6672](https://doi.org/10.3847/2041-8213/ac6672)

Event Horizon Telescope Collaboration, Akiyama, K., Alberdi, A., et al. 2022b, *ApJL*, 930, L13, doi: [10.3847/2041-8213/ac6675](https://doi.org/10.3847/2041-8213/ac6675)

Event Horizon Telescope Collaboration, Akiyama, K., Alberdi, A., et al. 2022c, *ApJL*, 930, L14, doi: [10.3847/2041-8213/ac6429](https://doi.org/10.3847/2041-8213/ac6429)

Event Horizon Telescope Collaboration, Akiyama, K., Alberdi, A., et al. 2023, *ApJL*, 957, L20, doi: [10.3847/2041-8213/acff70](https://doi.org/10.3847/2041-8213/acff70)

Event Horizon Telescope Collaboration, Akiyama, K., Alberdi, A., et al. 2024a, *ApJL*, 964, L26, doi: [10.3847/2041-8213/ad2df1](https://doi.org/10.3847/2041-8213/ad2df1)

Event Horizon Telescope Collaboration, Akiyama, K., Alberdi, A., et al. 2024b, *A&A*, 681, A79, doi: [10.1051/0004-6361/202347932](https://doi.org/10.1051/0004-6361/202347932)

Falcke, H., Körding, E., & Markoff, S. 2004a, *A&A*, 414, 895, doi: [10.1051/0004-6361:20031683](https://doi.org/10.1051/0004-6361:20031683)

Falcke, H., Körding, E., & Nagar, N. M. 2004b, *NewAR*, 48, 1157, doi: [10.1016/j.newar.2004.09.029](https://doi.org/10.1016/j.newar.2004.09.029)

Fender, R. P., Belloni, T. M., & Gallo, E. 2004, *MNRAS*, 355, 1105, doi: [10.1111/j.1365-2966.2004.08384.x](https://doi.org/10.1111/j.1365-2966.2004.08384.x)

Fishbone, L. G., & Moncrief, V. 1976, *ApJ*, 207, 962, doi: [10.1086/154565](https://doi.org/10.1086/154565)

Gallo, E., Fender, R. P., & Pooley, G. G. 2003, *MNRAS*, 344, 60, doi: [10.1046/j.1365-8711.2003.06791.x](https://doi.org/10.1046/j.1365-8711.2003.06791.x)

Gültekin, K., King, A. L., Cackett, E. M., et al. 2019, *ApJ*, 871, 80, doi: [10.3847/1538-4357/aaf6b9](https://doi.org/10.3847/1538-4357/aaf6b9)

Hankla, A., Philippov, A., Mbarek, R., et al. 2025, arXiv e-prints, arXiv:2512.01662, doi: [10.48550/arXiv.2512.01662](https://doi.org/10.48550/arXiv.2512.01662)

Heckman, T. M., & Best, P. N. 2014, *ARA&A*, 52, 589, doi: [10.1146/annurev-astro-081913-035722](https://doi.org/10.1146/annurev-astro-081913-035722)

Heinz, S., & Sunyaev, R. A. 2003, *MNRAS*, 343, L59, doi: [10.1046/j.1365-8711.2003.06918.x](https://doi.org/10.1046/j.1365-8711.2003.06918.x)

Hickox, R. C., & Alexander, D. M. 2018, *ARA&A*, 56, 625, doi: [10.1146/annurev-astro-081817-051803](https://doi.org/10.1146/annurev-astro-081817-051803)

Howes, G. G. 2010, *MNRAS*, 409, L104, doi: [10.1111/j.1745-3933.2010.00958.x](https://doi.org/10.1111/j.1745-3933.2010.00958.x)

Igumenshchev, I. V., Narayan, R., & Abramowicz, M. A. 2003, *ApJ*, 592, 1042, doi: [10.1086/375769](https://doi.org/10.1086/375769)

Inoue, Y., Khangulyan, D., Inoue, S., & Doi, A. 2019, *ApJ*, 880, 40, doi: [10.3847/1538-4357/ab2715](https://doi.org/10.3847/1538-4357/ab2715)

Jana, A., Ricci, C., Venselaar, S. M., et al. 2025, *A&A*, 699, A62, doi: [10.1051/0004-6361/202554491](https://doi.org/10.1051/0004-6361/202554491)

Kawamuro, T., Ricci, C., Imanishi, M., et al. 2022, *ApJ*, 938, 87, doi: [10.3847/1538-4357/ac8794](https://doi.org/10.3847/1538-4357/ac8794)

Kawazura, Y., Barnes, M., & Schekochihin, A. A. 2019, *Proceedings of the National Academy of Science*, 116, 771, doi: [10.1073/pnas.1812491116](https://doi.org/10.1073/pnas.1812491116)

Körding, E., Falcke, H., & Corbel, S. 2006, *A&A*, 456, 439, doi: [10.1051/0004-6361:20054144](https://doi.org/10.1051/0004-6361:20054144)

Kormendy, J., & Ho, L. C. 2013, *ARA&A*, 51, 511, doi: [10.1146/annurev-astro-082708-101811](https://doi.org/10.1146/annurev-astro-082708-101811)

Long, Q.-C., Dong, A.-J., Zhi, Q.-J., & Shang, L.-H. 2025, *ApJ*, 980, 187, doi: [10.3847/1538-4357/adaaee](https://doi.org/10.3847/1538-4357/adaaee)

Markoff, S., Nowak, M., Corbel, S., Fender, R., & Falcke, H. 2003, *A&A*, 397, 645, doi: [10.1051/0004-6361:20021497](https://doi.org/10.1051/0004-6361:20021497)

Merloni, A., Heinz, S., & di Matteo, T. 2003, *MNRAS*, 345, 1057, doi: [10.1046/j.1365-2966.2003.07017.x](https://doi.org/10.1046/j.1365-2966.2003.07017.x)

Mościbrodzka, M., Falcke, H., & Shiokawa, H. 2016, *A&A*, 586, A38, doi: [10.1051/0004-6361/201526630](https://doi.org/10.1051/0004-6361/201526630)

Narayan, R., Igumenshchev, I. V., & Abramowicz, M. A. 2003, *PASJ*, 55, L69, doi: [10.1093/pasj/55.6.L69](https://doi.org/10.1093/pasj/55.6.L69)

Narayan, R., & Yi, I. 1995, *ApJ*, 452, 710, doi: [10.1086/176343](https://doi.org/10.1086/176343)

Narayan, R., Yi, I., & Mahadevan, R. 1995, *Nature*, 374, 623, doi: [10.1038/374623a0](https://doi.org/10.1038/374623a0)

Netzer, H. 2015, *Ann. Rev. Astron. Astrophys.*, 53, 365, doi: [10.1146/annurev-astro-082214-122302](https://doi.org/10.1146/annurev-astro-082214-122302)

Özel, F., Psaltis, D., & Narayan, R. 2000, *ApJ*, 541, 234, doi: [10.1086/309396](https://doi.org/10.1086/309396)

Petrucci, P.-O., Piétu, V., Behar, E., et al. 2023, *A&A*, 678, L4, doi: [10.1051/0004-6361/202347495](https://doi.org/10.1051/0004-6361/202347495)

Plotkin, R. M., Markoff, S., Kelly, B. C., Körding, E., & Anderson, S. F. 2012, *MNRAS*, 419, 267, doi: [10.1111/j.1365-2966.2011.19689.x](https://doi.org/10.1111/j.1365-2966.2011.19689.x)

Prather, B. S. 2024, arXiv e-prints, arXiv:2408.01361, doi: [10.48550/arXiv.2408.01361](https://doi.org/10.48550/arXiv.2408.01361)

Quataert, E., & Gruzinov, A. 1999, *ApJ*, 520, 248, doi: [10.1086/307423](https://doi.org/10.1086/307423)

Rees, M. J., Begelman, M. C., Blandford, R. D., & Phinney, E. S. 1982, *Nature*, 295, 17, doi: [10.1038/295017a0](https://doi.org/10.1038/295017a0)

Ricarte, A., Gammie, C., Narayan, R., & Prather, B. S. 2023, *MNRAS*, 519, 4203, doi: [10.1093/mnras/stac3796](https://doi.org/10.1093/mnras/stac3796)

Ricci, C., Chang, C.-S., Kawamuro, T., et al. 2023, *ApJL*, 952, L28, doi: [10.3847/2041-8213/acda27](https://doi.org/10.3847/2041-8213/acda27)

Romero, G. E., Boettcher, M., Markoff, S., & Tavecchio, F. 2017, *SSRv*, 207, 5, doi: [10.1007/s11214-016-0328-2](https://doi.org/10.1007/s11214-016-0328-2)

Ruffa, I., Davis, T. A., Elford, J. S., et al. 2024, MNRAS, 528, L76, doi: [10.1093/mnrasl/slad167](https://doi.org/10.1093/mnrasl/slad167)

Shablovinskaya, E., Ricci, C., Chang, C.-S., et al. 2024, A&A, 690, A232, doi: [10.1051/0004-6361/202450133](https://doi.org/10.1051/0004-6361/202450133)

Sikora, M., & Begelman, M. C. 2013, ApJL, 764, L24, doi: [10.1088/2041-8205/764/2/L24](https://doi.org/10.1088/2041-8205/764/2/L24)

Singh, A., Bégué, D., & Pe'er, A. 2025, ApJL, 981, L11, doi: [10.3847/2041-8213/adb749](https://doi.org/10.3847/2041-8213/adb749)

Tchekhovskoy, A., Narayan, R., & McKinney, J. C. 2011, MNRAS, 418, L79, doi: [10.1111/j.1745-3933.2011.01147.x](https://doi.org/10.1111/j.1745-3933.2011.01147.x)

Volonteri, M., Sikora, M., & Lasota, J.-P. 2007, ApJ, 667, 704, doi: [10.1086/521186](https://doi.org/10.1086/521186)

Wang, Y., Wang, T., Ho, L. C., Zhong, Y., & Luo, B. 2024, A&A, 689, A327, doi: [10.1051/0004-6361/202449732](https://doi.org/10.1051/0004-6361/202449732)

Wong, G. N., Prather, B. S., Dhruv, V., et al. 2022, ApJS, 259, 64, doi: [10.3847/1538-4365/ac582e](https://doi.org/10.3847/1538-4365/ac582e)

Yarza, R., Wong, G. N., Ryan, B. R., & Gammie, C. F. 2020, ApJ, 898, 50, doi: [10.3847/1538-4357/ab9808](https://doi.org/10.3847/1538-4357/ab9808)

Yuan, F., Markoff, S., & Falcke, H. 2003a, Astronomische Nachrichten Supplement, 324, 453, doi: [10.1002/asna.200385044](https://doi.org/10.1002/asna.200385044)

Yuan, F., & Narayan, R. 2014, ARA&A, 52, 529, doi: [10.1146/annurev-astro-082812-141003](https://doi.org/10.1146/annurev-astro-082812-141003)

Yuan, F., Quataert, E., & Narayan, R. 2003b, ApJ, 598, 301, doi: [10.1086/378716](https://doi.org/10.1086/378716)

Zhang, X. A., Ricarte, A., Pesce, D. W., et al. 2025, ApJ, 985, 41, doi: [10.3847/1538-4357/adb45](https://doi.org/10.3847/1538-4357/adb45)